Microstructural Properties and in vitro Dissolution of Microporous Bioactive 13-93B3 Glass Powders Synthesized via Solution Combustion Synthesis

Negar Akrami[1,5+], Mehrnoosh Ghanad[1+], Philipp Keil[2], Henrik Bradtmüller[3,A*], Michael Ryan Hansen[2], Saeid Kargozar[4], Jalil Vahdati Khaki[1], Sahar Mollazadeh Beidokhti[1,B*]

[1] Department of Materials Engineering, Faculty of Engineering, Ferdowsi University of Mashhad (FUM), Azadi Sq., Mashhad, Iran

[2] Institute of Physical Chemistry, WWU Münster, Corrensstraße 28/30, D-41849 Münster, Germany

[3] Department of Materials Engineering, Vitreous Materials Laboratory, Federal University of São Carlos, CP 676, 13565-905, São Carlos, SP, Brazil

[4] Tissue Engineering Research Group (TERG), Department of Anatomy and Cell Biology, School of Medicine, Mashhad University of Medical Sciences, Mashhad 917794-8564, Iran

[5] Department of Biomedical Engineering, The State University of New York at Stony Brook, Stony Brook, NY, United States

+These authors contributed equally.

* Corresponding Authors:
E-Mail[A*]: mail@bradtmueller.net
E-Mail[B*]: mollazadeh.b@um.ac.ir

Abstract

This study investigates the bioactivity and microstructural properties of borate-based bioactive 13-93B3 glass produced by the solution combustion synthesis (SCS) method using urea and sucrose fuels at different reaction temperatures. The results show that these glasses exhibit unique properties compared to conventionally-synthesized borate-based bioactive glasses. The glass particles produced have porous surfaces, with particle size below 100 nm. BET measurements reveal that the mesoporous structure of these glasses is characterized by high-specific surface areas, promoting a high ion release and hydroxyapatite layer formation in simulated body fluid (SBF). The crystallization of the amorphous calcium phosphate was investigated by ^{1}H, ^{31}P MAS, and 2D ^{31}P{1H} heteronuclear correlation (HETCOR) spectroscopy, showing that it progresses linearly up to three days. The produced glasses were tested for their effects on the viability of 3T3 cells and were found to have no toxic effects. Therefore, the produced glasses are promising candidates for tissue engineering applications.

1. Introduction

Since the first report on bioactive glasses in 1971 [1], the research interest in the field of synthesis and application of bioactive glasses and ceramics has attracted considerable attention from both industry and academia [2–4]. The field's maturation is reflected in the many studies showing the unique ways that these materials can be used to replace, regenerate, or repair damaged parts of the human body [4–6]. The earliest application of bioactive glasses was aimed at hard-tissue regeneration [5–9]; however, over the last few decades, their use was successfully expanded to soft-tissue replacement applications [10–13]. Borate-based bioactive glasses are especially notable among the known bioactive glass compositions due to their high reactivity and stimulative effect on the angiogenesis process [11,14,15]. Recently, exciting novel applications in wound healing were found, where these glasses can function as advanced wound matrices in the form of bioabsorbable glass fibers and beads [15,16]. For this application it is essential that the biomaterial can release functional ions, such as calcium, sodium, potassium, and boron, from borate-based bioglasses during immersion in the physiological solutions to be ultimately absorbed from the tissue. The above-mentioned ions play an essential role in cellular processes associated with tissue regeneration, i.e., angiogenesis and antibacterial activity. For example, the reaction between released Ca^{2+} and PO_4^{3-} ions in the medium leads to the precipitation of amorphous calcium phosphate (ACP), which eventually crystallizes to HA [14]. However, the extent of ion release from the bioactive glass should occur in optimal concentrations at specific times to be able to activate a sustainable and desirable cellular response [17]. For borate-based bioglasses, the release of functional ions is controllable to a large extent by manipulating the composition and microstructure of the parent glass [18–21]. Particle size distribution, specific surface area, and

porosity, which are all strongly governed by the applied synthesis method, are some important microstructural factors affecting the rate of ion release in the aqueous media.

The production of borate bioactive glasses is conventionally carried out through melt-quenching and sol-gel techniques. Despite the progress that has been made with these methods, there are still challenges to overcome. For instance, the melt-quenching method requires expensive equipment such as high-temperature furnaces and often noble metal crucibles [22–25]. While the sol-gel method has some promising advantages, such as the ability to produce glasses with increased surface area and nanoporosity [26], it is generally rather time-consuming and requires a high degree of chemical expertise, which is prohibitive for large-scale industrial applications. Finally, the resulting glasses may not have the desired structural homogeneity, particularly for glasses that contain components with high chemical affinity [27]. To overcome these challenges, it was shown recently that the solution combustion synthesis (SCS) method might serve as a promising alternative. [28] Thus, it was recently [28] demonstrated by some of the authors of the present manuscript that solution-SCS can produce nanoporous borate-based 13-93B3 glass powders due to the high volume of gaseous by-products released during the combustion reaction. The advantages of the SCS method lie in the minimal equipment requirements and the possibility of using inexpensive raw materials, making it more sustainable, more resource-conscious, and more economical than traditional methods. Overall, this method is straightforward and fast and can be used for large-scale synthesizing procedures [19,29].

The two major factors of the SCS process affecting the final physical and microstructural properties are the combustion temperature and the gas release rate. Generally, high enough combustion temperatures result in the rapid release of large amounts of gases, which produces fine particle size distributions and porous glass powders with low density [30].

Based on the above considerations, the present contribution focuses on a deeper understanding of the physical and chemical properties of glass powders, previously prepared *via* the SCS method by some of the authors [28]. As it was pointed out in that work[28], the effect of [30]synthesis temperatures T_0 and fuels on the phase and structural groups contribution of the produced glass powders were investigated, where urea was chosen as one of the most commonly employed fuels in SCS process [30], and sucrose was investigated as an alternative fuel whose potential residuals may be digestible by the human body. In contrast, the current research focuses on T_0, which is a proxy for the sum of complex synthesis parameters, and its relationship to the microstructural and bioactivity properties of the synthesized powders. To this end, the microstructural properties of the samples are investigated through dynamic light scattering (DLS), physisorption, and solid-state NMR spectroscopy. Further, *in vitro* bioactivity studies were carried out by the characterization of the glass dissolution process in the simulated body fluid (SBF) *via* ICP-OES, powder x-ray diffraction, and cell viability studies. The results show that 13-93B3 bioactive glass nanoparticles produced using urea and sucrose as SCS fuels are promising candidates for tissue engineering applications due to the fast release of therapeutic ions and HA layer formation.

2. Materials and methods

2.1. Sample preparation

13-93B3 glass powders (with the nominal composition of $54.6B_2O_3$–$6Na_2O$–$7.9K_2O$–$7.7MgO$–$22.1CaO$-$1.7P_2O_5$ %mol) were prepared through solution combustion synthesis (SCS) according to a recently described procedure [28]. In summary, all raw materials were dissolved in deionized water and thoroughly mixed with either sucrose or urea as fuels in controlled ratios. Table 1 lists the purity of the starting materials used in the syntheses. The homogeneous solutions were then placed inside a box furnace at 400, 500, 600, 700, 750, and 800 °C, where the combustion reaction occurred spontaneously after the solvent's complete evaporation. The final products were obtained as voluminous glass powders.

Table 1: Starting materials employed for the synthesis of 13-93B3 glass powders.

Compound name	Chemical formula	Supplier	Purity (%)
Phosphoric acid 85%	H_3PO_4	Sigma-Aldrich, USA	≥99.99%
Boric acid	H_3BO_3	Sigma-Aldrich, USA	≥99.50%
Calcium nitrate tetrahydrate	$Ca (NO_3)_2 \cdot 4H_2O$	Sigma-Aldrich, USA	≥99.00%
Magnesium nitrate hexahydrate	$Mg (NO_3)_2 \cdot 6H_2O$	Sigma-Aldrich, USA	99.00%
Potassium nitrate	KNO_3	Sigma-Aldrich, USA	≥99.00%
Sodium nitrate	$NaNO_3$	Sigma-Aldrich, USA	≥99.00%
Urea	NH_2CONH_2	Sigma-Aldrich, USA	≥99.00%
Sucrose	$C_{12}H_{22}O_{11}$	Sigma-Aldrich, USA	≥99.50%

2.2. Microstructural characterization

Particle size distributions were measured *via* dynamic light scattering (DLS) using a Vasco3 DLS system (Cordouan, France). To this end, 10 mg of each glass powder was dispersed in 10 mL of absolute ethanol in an ultrasonic bath (FR USC 22 LQ, 400 w, 20%, Taiwan) for 5 min.

Physisorption measurements were performed on a BELSORP MINI II volumetric adsorption analyzer at -196 °C (77 K). Samples were degassed at 250 °C for 24 h under reduced pressure before each measurement. Finally, the specific surface areas of the glass powders were characterized according to the Brunauer-Emmett-Teller (BET) and Barrett-Joyner-Halenda (BJH) analysis (BET BELSORP-MINI II, Japan).

2.3. *In vitro* bioactivity studies

The bioactivity of the synthesized glass powders was tested using simulated body fluid (SBF) prepared according to the Kokubo method [17]. The samples were immersed in a shaker incubator for 3, 7, 24, and 72 h in the SBF medium (glass powder to liquid ratio = 1.5 mg/mL) at 37 °C. After three days of immersion, the samples were rinsed with acetone (Merck, Germany) and dried under atmospheric conditions at 50 °C. Moreover, after each immersion period, the pH was determined, and the concentrations of BO_3^{3-}, Ca^{2+}, Mg^{2+}, K^+, and PO_4^{3-} ions released in the SBF media were measured by inductively coupled plasma optical emission spectrometry (ICP-OES Thermo Scientific iCAP 6500).

Powder X-ray diffraction (XRD) was used to detect the crystalline phases in the pristine glass powders and after their immersion in SBF. Measurements were done on a GNR X-Ray diffractometer employing Cu-K_α radiation (λ = 1.54 Å) at 40 kV and 30 mA. The 2θ range of 20

to 80° was probed at room temperature with step-scanning in steps of 0.01° and an integration time of 2 s.

The morphology of glass powders was analyzed three days after immersion in SBF using FESEM microscopy, performed on a MIRA3, TESCAN microscope using an accelerating voltage of 15 kV after sputter-coated the samples with gold for 180 s.

2.3.1 NMR Studies after SBF-immersion

Solid-state ^{31}P and ^{11}B MAS NMR and 2D ^{31}P{^{1}H} heteronuclear correlation (HETCOR) MAS NMR measurements were conducted to investigate the effects of dissolution on the glass structure and the formation of HA after SBF immersion. The ^{31}P direct excitation MAS NMR measurements were performed on a Bruker DRX 200 spectrometer operating at a magnetic flux density of $B_0 = 4.7$ T with a 4 mm H/X DVT MAS probe. For the pristine S750 sample, 5280 scans were acquired at a relaxation delay of 60 s. 7.5 µs π/2-pulses were used for excitation ($\nu_{nut} = 33.3$ kHz), and the sample was spun at $\nu_{MAS} = 8$ kHz. For each ^{31}P MAS NMR spectrum of the SBF-immersed samples, 384 scans were acquired using 2.9 µs π/2-pulses ($\nu_{nut} = 86.2$ kHz), at a spinning rate of $\nu_{MAS} = 10$ kHz. Additionally, ^{31}P MAS NMR spectra of pristine Hydroxyapatite nanopowder (Sigma-Aldrich, >97%, <200 nm particle diameter) were recorded to estimate the required relaxation delay for crystalline HA species. A relaxation delay of 128 s was found to be sufficient for quantitatively detecting crystalline HA species and thus used for all ^{31}P MAS NMR spectra of SBF-immersed glasses.

Additionally, ^{11}B EASY MAS NMR [31,32] measurements were performed on a Bruker DSX 500 spectrometer operating at $B_0 = 11.74$ T with a 4 mm H/X/Y DVT MAS NMR probe. 4800 scans were acquired using 0.3 µs excitation pulses ($\nu_{nut} = 83.3$ kHz, 9° flip angle w.r.t. liquid standard),

relaxation delays of 32 s, and a saturation comb before each excitation pulse to ensure that the sample signal is saturated during the second acquisition period of the EASY sequence. Hahn echo ^{1}H MAS NMR, and 2D ^{31}P{^{1}H} HETCOR MAS NMR [33,34] spectra were recorded on a Bruker Avance III spectrometer using $\nu_{MAS} = 12.5$ kHz, a relaxation delay of 1 s (chosen based on inversion recovery experiments not shown here), and nutation frequencies of $\nu_{nut,P} = 78.3$ kHz and $\nu_{nut,H} = 65.8$ kHz for ^{31}P and ^{1}H, respectively. The Hartmann-Hahn matching condition $\nu_{nut,H} = \nu_{nut,P} + n\nu_{MAS}$ with n=1 was optimized directly for the sample by variation of the power level applied to the ramped contact pulse on the ^{31}P channel. For the 2D HETCOR MAS NMR spectra, 64 increments were recorded with 16 scans using the States-TPPI protocol [35]. Swept-frequency two-pulse phase modulation (SW^f-TPPM) [21] was applied during acquisition to the proton channel for decoupling, and CP contact times were varied from 0.1 ms to 7.0 ms. For all measurements, Adamantane (Aldrich, 99+%, $\delta_{iso} = 1.85$ ppm), H$_3$PO$_4$ (Riedel deHaën, 85 wt.%, $\delta_{iso} = 0$ ppm) and BF$_3 \cdot$ OEt$_2$ (Merck, $\delta_{iso} = 0$ ppm) were used as chemical shift references for ^{1}H, ^{31}P, and ^{11}B, respectively. All NMR datasets were processed with Bruker TopSpin 4.0.9. Deconvolutions were performed in ssNake 1.4b [36] using the Powell minimization method and assuming mixed Gaussian-Lorentzian lineshapes (except for the component P_1^{HA} which was assumed to be purely Lorentzian).

2.3.2 Cell viability studies

Fibroblast cell line 3T3 mouse cells used in the experiments were provided by the National Cell Bank of Iran (Pasteur Institute of Iran). The cells were seeded in DMEM high glucose medium supplemented with 10% Fetal Bovine Serum (FBS) and 1% penicillin/streptomycin (Pen/Strep) solution (Gibco, Waltham, MA, USA) in a 96-wells plate (SPL Lifesciences, South Korea) (5 $\times$ 10^3 cells/well). Once 70% confluence was attained, the cells were subcultured for the cytotoxicity

study. All cell cultures were conducted at 37 °C in a humidified atmosphere of 5% CO_2. The effect of the produced bioglass powders on the 3T3 Cell viability was evaluated using standard colorimetric 3-(4,5-dimethylthiazol-2-yl)-2,5-diphenyltetrazolium bromide MTT assays (Sigma-Aldrich, St. Louis, MO, USA). The conditioned medium was prepared by adding 0.5, 1, and 2.5 mg of the UV-sterilized glass powders to 1 mL of the culture medium (DMEM high glucose supplemented by 10% FBS and 1% Pen-Strep). The culture media containing bioactive glass powders was filtered through 0.22 μm pore size filters (Jet Bio-Filtration Co., China) and was replaced with a culture medium after 24 h for cell culture in a 96-well plate. After 24 h, the culture media containing glass powders were removed, and the MTT solution (5 mg/mL) was added to the plate wells. After incubating the plate for four hours, all media was extracted with dimethyl sulfoxide (DMSO, Sigma-Aldrich, St. Louis, MO, USA). Finally, the plate well's Optical Density (OD) was measured by a microplate reader (Synergy HT, BioTek, USA) at 570 nm. The subsequent numerical analysis was performed on three samples, and the output results are shown as mean ± standard deviation (SD). After that, statistical analysis was performed using the one-way ANOVA analysis in the GraphPad Prism framework. In this step, probability values less than 0.05 were considered statistically significant. (* $p < 0.05$, ** $p < 0.01$, *** $p < 0.001$, and **** $p < 0.0001$).

3. Results and discussion

3.1 Microstructural Characterization

Particle size distributions

The mean particle size of the synthesized glass powders in the presence of urea and sucrose as fuels are displayed in Figures 1 and 2, respectively. In addition, the particle size distributions of all samples are summarized in Table 2[19][37]. Based on the results of Table 2, it can be observed that the mean particle size of synthesized glass powders is relatively independent of the initial temperature of the furnace (T_0: 400 to 700 °C). However, a significant increase in the mean particle sizes can be observed beyond 700 °C and 750 °C for the urea and sucrose systems, respectively.The increase can be attributed to the sintering of the produced glass particles above those threshold temperatures [30]. Particle sizes for specimens synthesized with sucrose as fuel (see Figure 2) decrease slightly when raising T_0 above 400 °C but reach values comparable to the other system over the T_0 range of 600 to 750 °C. Again, the same drastic increase in mean particle size is observed beyond this temperature. It has to be noted that the size distributions for the urea system are overall much narrower than those of the sucrose system, indicating a more controlled reaction. Therefore, the observed differences in the mean particle size values appear to depend to some degree on the gas release during the SCS reaction [30].

The DLS results demonstrate that synthesized samples using the SCS method have a particle size distribution in which a significant proportion of particles are below 100 nm. In comparison, conventional methods of melt quenching and sol-gel produce glass powders with mean particle sizes of 2-5 µm and 105 nm, respectively [37,38].
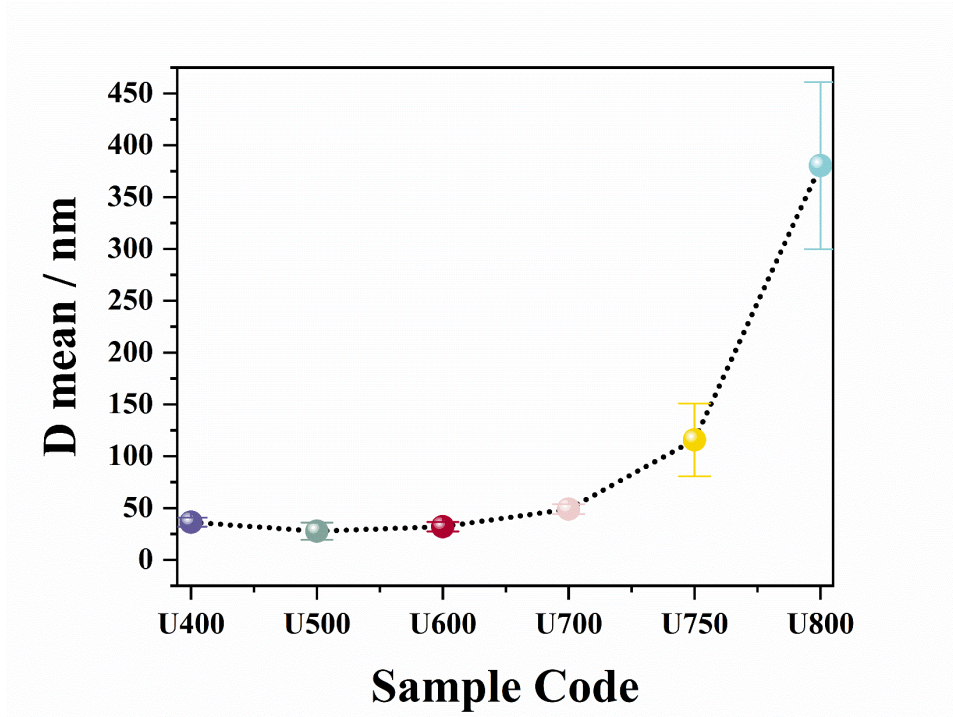
Figure 1. The mean particle sizes of the synthesized glass powders in the presence of urea as a fuel by T_0.
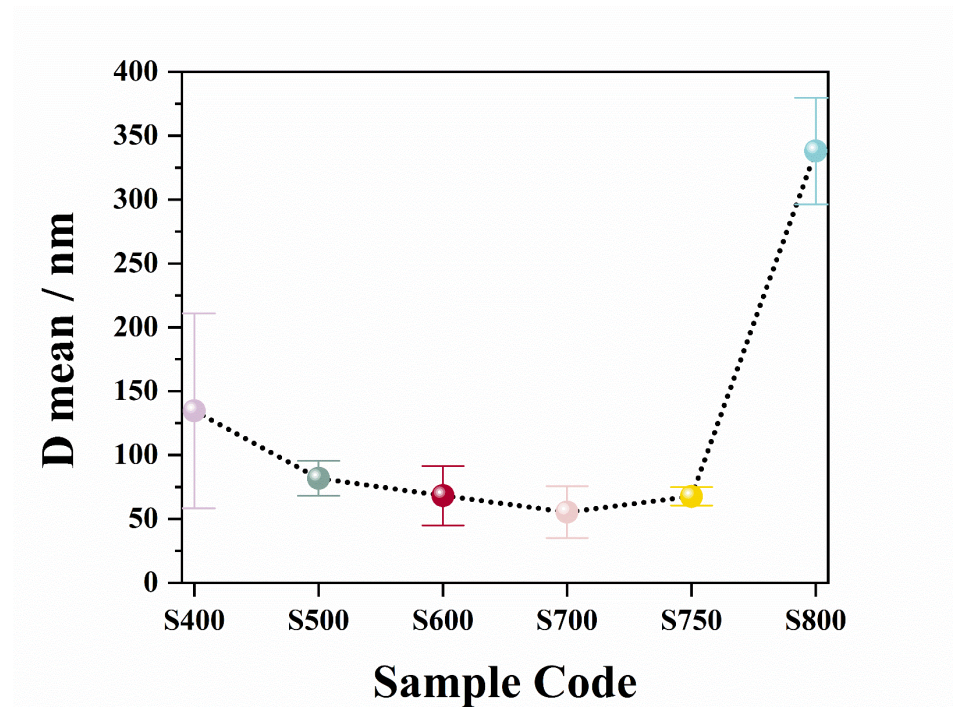

Figure 2 The mean particle sizes of the synthesized glass powders in the presence of sucrose as a fuel by T_0.

Table 2. The particle size distribution of 13-93B3 glass powders synthesized using urea (top) and sucrose (bottom) as reaction fuels.

Samples code / particle size (nm)	U400 / %	U500 / %	U600 / %	U700 / %	U750 / %	U800 / %
0-20	9	31	17	0	0	0
20-40	61	55	61	44	4	0
40-60	21	11	17	34	26	0
60-80	5	2	3	13	19	0
80-100	2	1	2	5	13	4
100-120	2	0	0	3	8	3
120-140	0	0	0	1	5	3
140-160	0	0	0	0	4	3
160-500	0	0	0	0	18	67
500-1000	0	0	0	0	3	20
Samples code / particle size (nm)	S400 / %	S500 / %	S600 / %	S700 / %	S750 / %	S800 / %
0-20	0	0	0	0	0	0
20-40	0	5	31	38	26	0
40-60	32	30	34	34	34	0
60-80	19	26	15	15	17	4
80-100	11	17	7	7	9	6
100-120	6	9	5	3	4	5
120-140	4	4	4	2	4	4
140-160	3	4	4	1	3	4
160-500	22	3	0	0	3	63
500-1000	3	2	0	0	0	14

Physisorption measurements

Figures 3 and S1 in the supporting information section show the measured nitrogen adsorption/desorption isotherms at 77 K and the corresponding BET isotherms of the synthesized glass powders in the presence of urea and sucrose as fuels, respectively. Table 3 lists the specific parameters obtained from BET (surface area S_{BET}, total pore volume) and BJH analysis (average pore diameter(nm), dBJH plot) of the measurements. According to the IUPAC classification, the nitrogen adsorption/desorption isotherms of the investigated samples are of type III with an H3 hysteresis loop that confirms the mesoporosity of the glass particles [46].
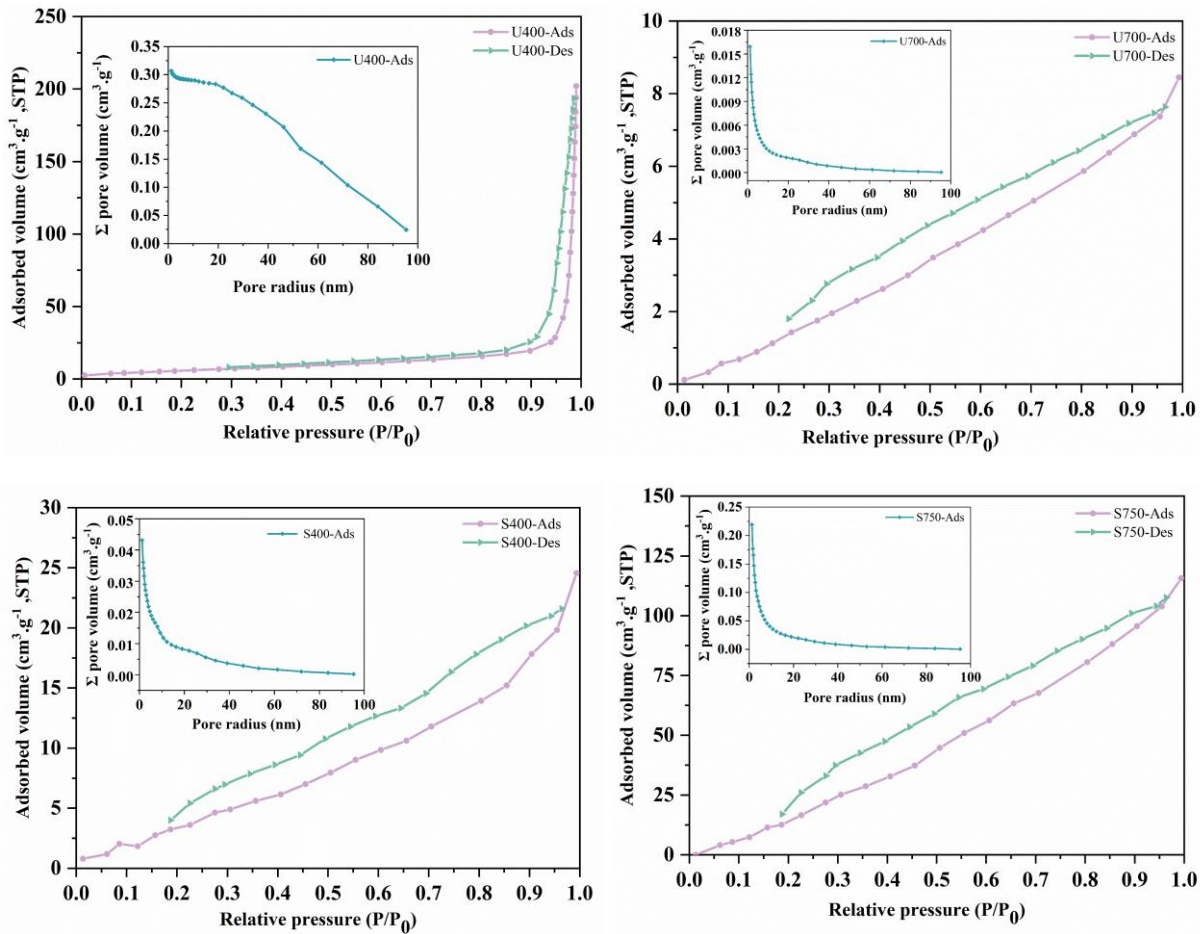
Figure 3. BET isotherms for samples U400 (top left), U700 (top right), S400 (bottom left), and S750 (bottom right). Note the different vertical scales of the measurements.

For all samples, except the S750 sample, moderate specific surface areas between about 10 and 23 m²/g are observed, which are lower than those of powders produced by the sol-gel method, which lie in the range of about 25 to 300 m²/g [26,39,40]. Typically, with SCS, it is possible to obtain nanopowders with even higher surface areas; however, it seems for this borate-based composition, some sintering or agglomeration at the employed combustion temperatures may reduce the surface areas. All samples exhibit mesopores (2-50 nm), except the U400 sample, whose pores can be classified as macropores (>50 nm) [26,39–41].

Table 3. Parameters obtained from BET (S_{BET} (m²/g), the total pore volume (cm³/g)), and BJH analysis (average pore diameter (nm)) on the samples under study.

Samples	BET		BJH
	Specific surface area S_{BET} (m²/g)	Total pore volume (cm³/g)	Average pore diameter (nm)
U400	23.08	0.305	25
U700	10.77	0.013	21
S400	22.37	0.037	20
S700	10.01	0.019	21
S750	186.60	0.177	25

According to Figure 3 and Table 3, the surface area significantly decreased by increasing the fuel/nitrates ratio (the explicit calculation is shown elsewhere)[28]. This indicates that higher oxidant levels provide a more favorable gas release resulting in higher mesoporosity. For S750, the experiments yield a specific surface area of 186 m²/g, which is significantly higher than for the other synthesized samples. While we prefer to refrain from a tentative explanation of the increased surface area's origin, this result indicates that additional fine-tuning of the synthesis conditions may produce powders with further increased specific areas. Overall, the above results demonstrate that SCS produces glass powders with mesoporous microstructures. In the following, the dissolution behavior of some selected samples, the rate of apatite layer formation, and finally the effect of the glasses' morphology on the bioactivity assessment are discussed.

3.2 Functional Characterization

Dissolution behavior of glass powders in SBF

Ion-concentrations of Ca^{2+}, K^+, Mg^{2+}, Na^+, PO_4^{3-}, and BO_3^{3-} after immersion of the prepared glass powders in SBF for 3, 7, 24, and 72 hours are shown in Figures 4 and S2 to S6, respectively. The dissolution profiles are quite similar for the urea and sucrose series samples. One of the main

differences is the total amount of released boron, calcium, and magnesium ions after 72 h of immersion time. As mentioned in the PSA section, the particle size distribution of the synthesized glass powders with urea is smaller, potentially favoring higher ion release rates compared to the samples synthesized in the presence of sucrose fuel [18].
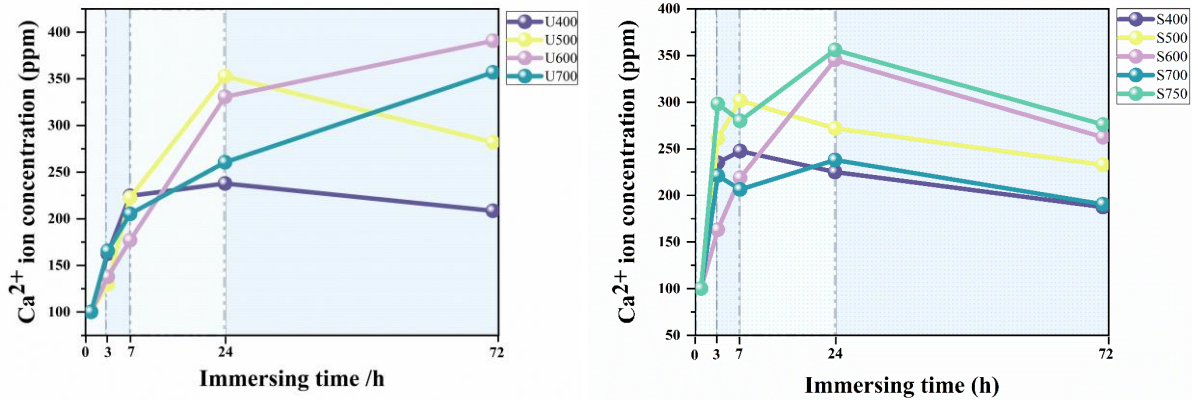

Figure 4. Ca^{2+} ion concentration of synthesized glass powders in the presence of urea (left) and sucrose (right). (purple=X400, yellow=X500, pink=X600, blue=X700, green=X750 with X = U, S)

According to Figure 4, the release rate of Ca^{2+} ions from the U/S400 samples during the first 7 hours was rapid and then plateaued in the next 7-24 hours. Finally, after 24 hours, some Ca^{2+} absorption can be observed for the U/S400 samples. The U/S500 samples follow a similar trend; however, there is a steeper increase in the Ca^{2+} concentration until 24 hours. On the other hand, the U/S600, U/S700, and S750 samples showed a rapid Ca^{2+} release up to the first 24 hours, which then slightly decreased, but only U600 and U700 did not indicate Ca^{2+} absorption after 24 h. The decrease of Ca^{2+} ion concentrations could be attributed to the formation of an HA layer on the surface of the samples, which will be discussed below. The SCS-synthesized glass powders in the current research released up to 309.50 ppm Ca^{2+} ions in 72 h, which is significantly more than reported for powders synthesized through melt quench or sol-gel methods, reported as 130.25 ppm

and 90 ppm, respectively [38,42]. The faster release of Ca^{2+} ions produced by the SCS method could be a consequence of the narrow particle size range (10-85 nm) of the final powders. The U600 and U700 samples showed maximum concentrations of released Ca^{2+} ions in the SBF medium.

Figure S4 shows that the PO_4^{3-} concentration in SBF decreases continuously for all samples with increasing immersion periods, which is owed to the formation of the HA phase, which consumes PO_4^{3-} [43]. Liu et al. [42] reported that the PO_4^{3-} ion concentrations in SBF were about 74.33 ppm and 20 ppm after three days of immersion in SBF for a bioactive 13-93B3 glass microfiber and glass powders, respectively, synthesized by the sol-gel method [38]. About 2.6 ppm of PO_4^{3-} ions were released in the samples discussed in the present study during the same period.

As shown in Figure S5, the BO_3^{-3} ion concentration evolves analogously to the Ca^{2+} ions, without the re-absorption at higher times. Among all the samples, the U600 and U700 samples have the highest concentration of BO_3^{-3} ion released in SBF, which is 326 ppm. According to prior XRD studies [28], these samples are free of crystalline phases. Figure S2 and Figure S3 display that the release of K^+ and Mg^{2+} ions increases with increasing immersion time. All samples exhibit a two-step increase: first, a steep increase during the first three hours, followed by another, albeit somewhat slower, increase between 24 and 72 hours. Similar behavior is found in the pH of the SBF solution. Dissolution of the glass of components (e.g., K_2O, Na_2O, B_2O_3) into the SBF and forming a HA layer causes changes in the pH values [44]. Figure 5 shows the pH alterations as a function of immersion time for the urea and sucrose systems.
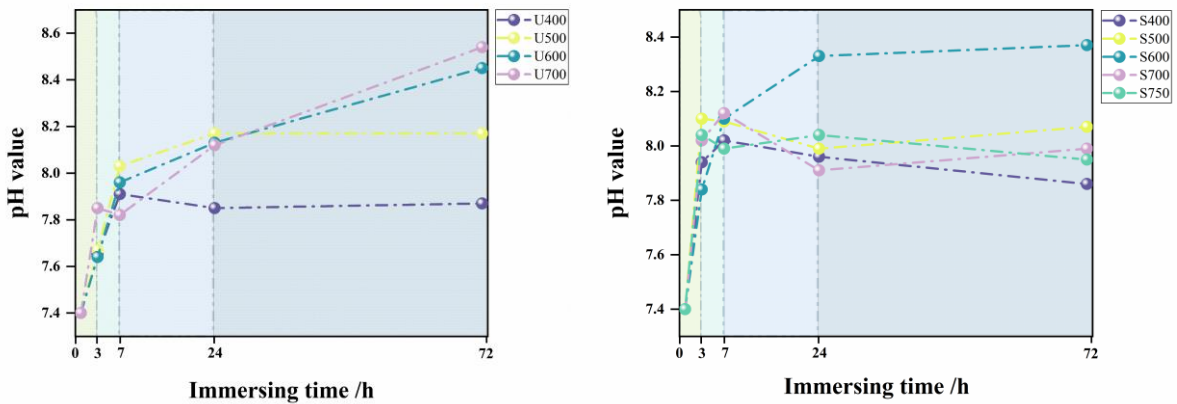
Figure 5. Dependence of pH values of SBF and the immersion time in the investigated glass powders using urea (left) and sucrose (right) as fuel.

Overall, the pH values increase with immersion time similarly for all samples and appear correlated principally to the K^+ concentration. However, the pH values of the samples have not reached a plateau value after 72 h. In summary, it is worth pointing out that while the SCS produced glass powders have similar or lower specific surface areas than sol-gel produced 13-93B3 glass powders, the ion concentrations after immersion in SBF for 24 h of K^+, Mg^{2+}, BO_3^{3-}, and PO_4^{3-} are about 3, 2.5, 1.5, and 1.4 times higher compared the sol-gel specimens [38]. Several factors can be imagined to govern the ion release rate apart from the specific surface area: The samples prepared by the SCS method, for example, exhibit smaller particle sizes compared to those synthesized through the sol-gel method[https://doi.org/10.3390/BIOENGINEERING9090442.] and are likely to feature a different boron speciation, i.e., the share of B3 and B4 units [28]. We base this on our previous observation that the boron speciation of SCS-prepared glasses may differ significantly from those of melt-quench 1393-B3 glass[37] depending on the used synthesis temperature [28]. BO^{3-} and BO^{4-} units have different stabilities in aqueous solutions that also depend on the pH of the solution[https://doi.org/10.1016/j.jnoncrysol.2015.07.003.] (especially in the pH range of 7.4 and 8.4, see Figure 5), which may increase the amounts of released BO^{4-}. Lastly, not only the boron

speciations may differ between SCS and sol-gel glasses, but also the different intermediate-range structures of the network formers.

XRD investigation after SBF-immersion

Powder X-ray diffraction was used to detect crystalline HA in the bioactive glass powders after 72 hours in SBF. Figures 6 and 7 show diffractograms of the glass powders in the presence of urea and sucrose before and after being immersed in the SBF, respectively. While in the pristine samples, no diffraction bands can be observed (compared with Figure 6), Figure 7 (left) clearly shows a principal peak at $2\theta = 32°$ (ICDD96-431-7044), corresponding to HA in the U500-U700 samples. With increasing the synthesis temperature (T_0), the diffraction peaks become increasingly narrow, indicating larger crystallites are found in U700, attributable to higher solution pH values, which generally facilitate apatite nucleation, and the larger mean particle sizes of the specimen [40]. Figure 7 (right) shows the HA phase at $2\theta = 32°$ (ICDD96-431-7044) for the S500-S700 samples, and demonstrates that the S700 sample has more intense peaks related to the HA phase, which indicates some differences in the morphology of S700 compared to the other samples. Another possible reason is its smaller particle size than those of S500 and S600, which increased the ion release rates in the S700 sample and thus led to different crystallization dynamics [18]. The XRD patterns of the samples synthesized in the presence of urea show more intense bands related to HA after immersion in SBF, than those synthesized with sucrose. This agrees with the ICP-OES data, showing a higher Ca^{2+} release, favoring higher HA formation.
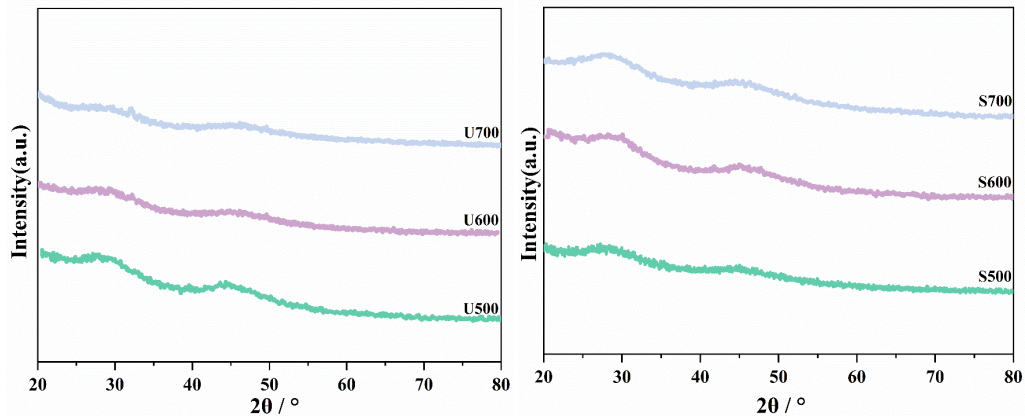
Figure 6. Powder x-ray diffractograms of U500, U600, and U700 (left) and S500, S600, and S700 (right) before immersion in SBF [28].
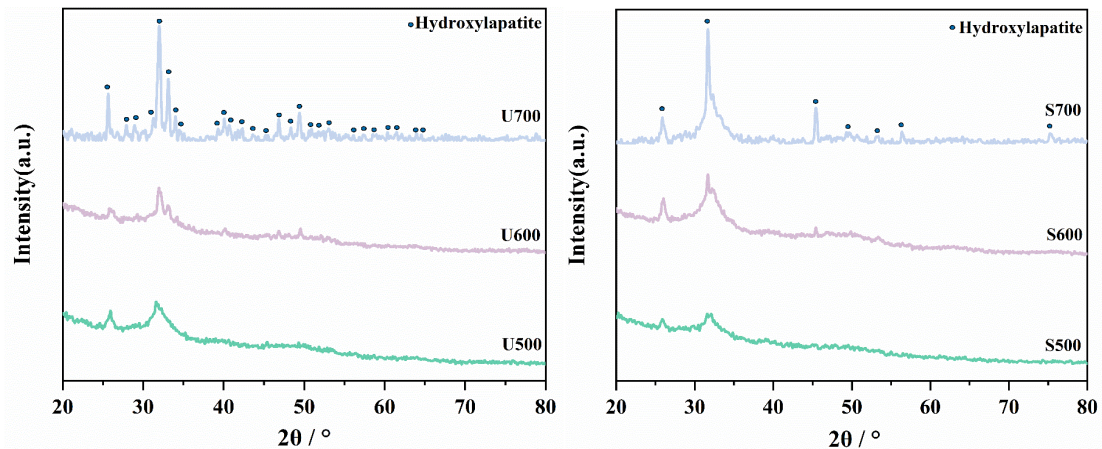

Figure 7. Powder x-ray diffractograms of U500, U600, and U700 (left) and S500, S600, and S700 (right) after three days of immersion in SBF.

FESEM investigation after SBF-immersion

The FESEM micrographs of the synthesized samples in the presence of urea and sucrose as fuels before and after immersion in the SBF media for 72 hours are represented in Figures 8 and 9, respectively. FESEM results confirm that the mineralized phases have two different morphologies. The differences could be related to the different ion release rates of the samples, leading to different crystallization mechanisms. Additionally, since the fuel type affects the morphology, porosity, and

surface area, some effect on the formation of the HA phase with different morphologies is likely[19].
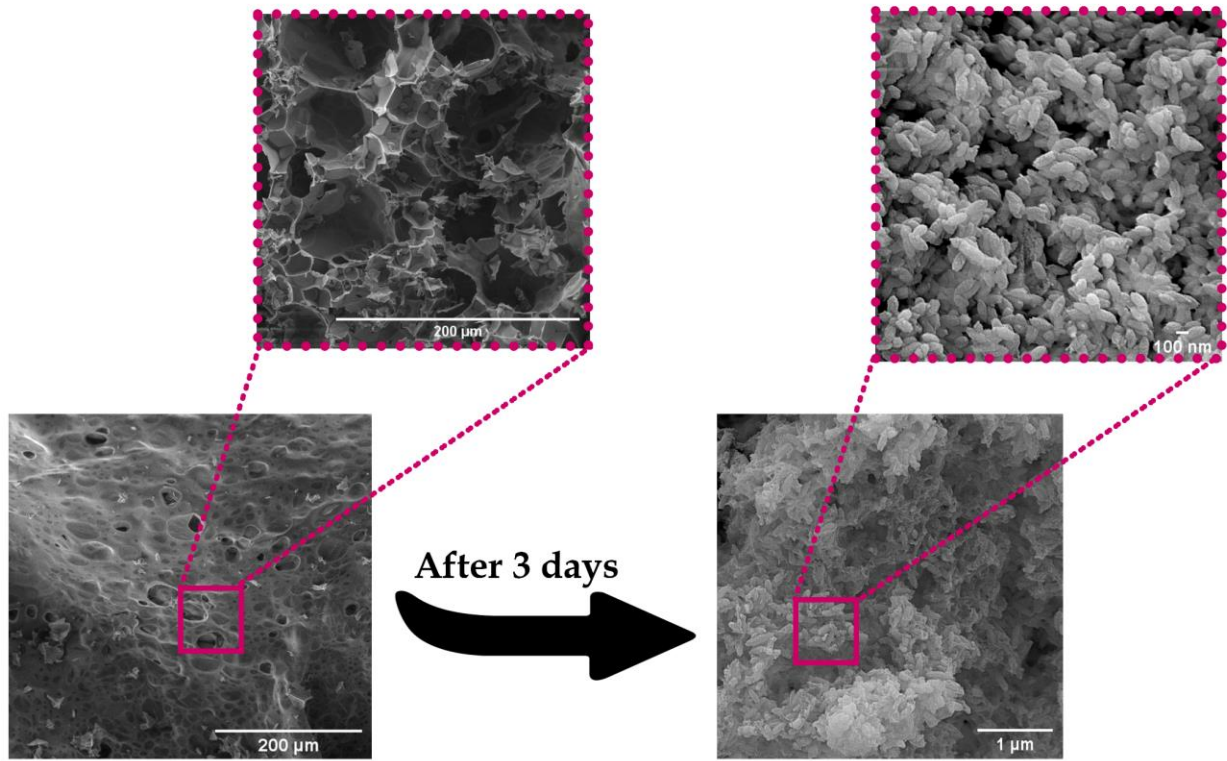
Figure 8. FESEM of U700 (left) and after three days of immersion in SBF(right).
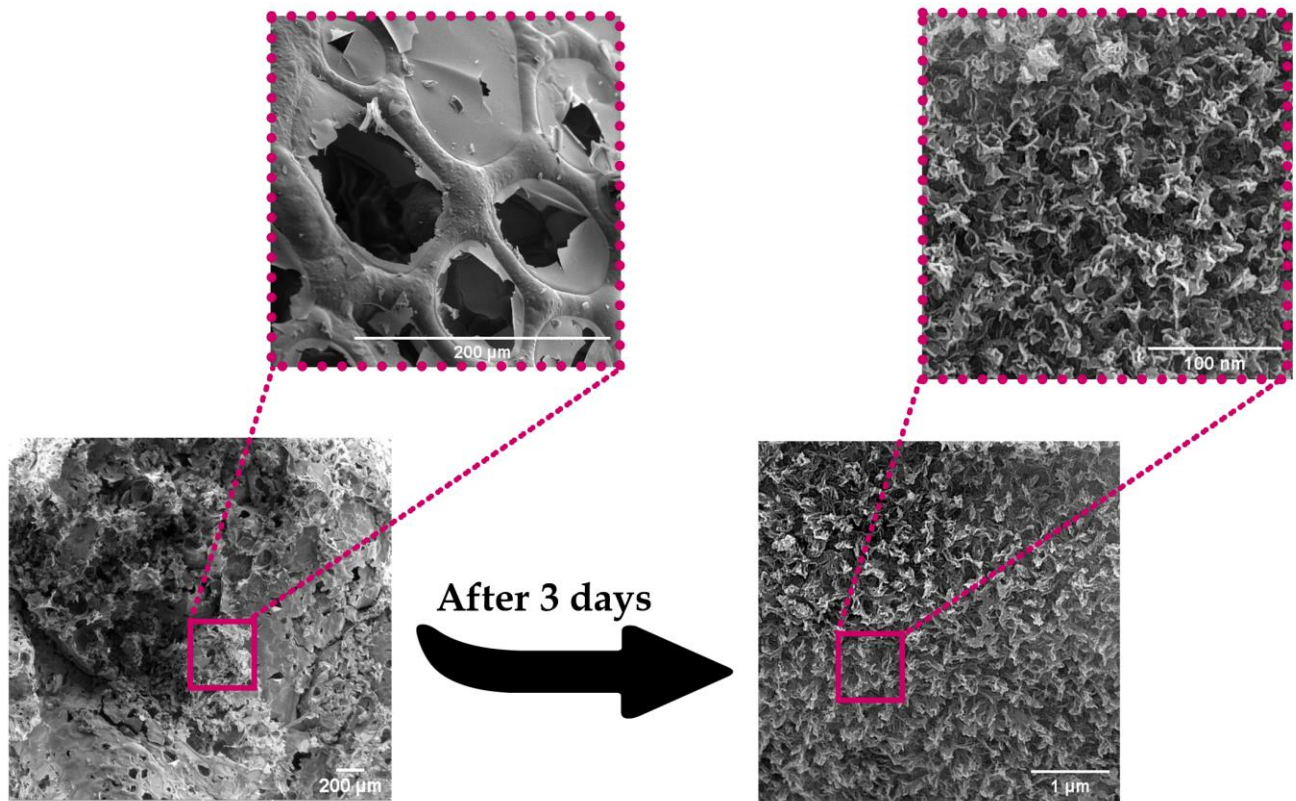
Figure 9. FESEM of S700 (left) and after three days of immersion in SBF (right).

Solid-State NMR investigation after SBF-immersion

The acquired ^{31}P MAS NMR spectra of pristine HA nanoparticles as well as S750 after different periods of immersion in SBF, are shown in Figure 10(a). As was previously reported in other studies [45,46], pristine HA is observed as a combination of one sharp signal at $\delta_{\mathrm{iso}} = 2.3$ ppm and a low-intensity shoulder at $\delta_{\mathrm{iso}} = 5.3$ ppm. For all SBF-immersed samples, broader and more asymmetric ^{31}P signals w.r.t. pristine HA with $\delta_{\mathrm{iso}} = 2.5$ ppm are detected, indicating the presence of tetragonally symmetric PO_4^{3-} anions (i.e., Q^0 units). Furthermore, for immersion times below one day, the signal is slightly asymmetric, indicating that another shoulder is present, which may either be caused by a range of hydrogenated calcium phosphates or by the glassy phosphate

species of the 13-93B3 structure found in S750 before immersion (also shown in Figure 10(a) as a dashed line).
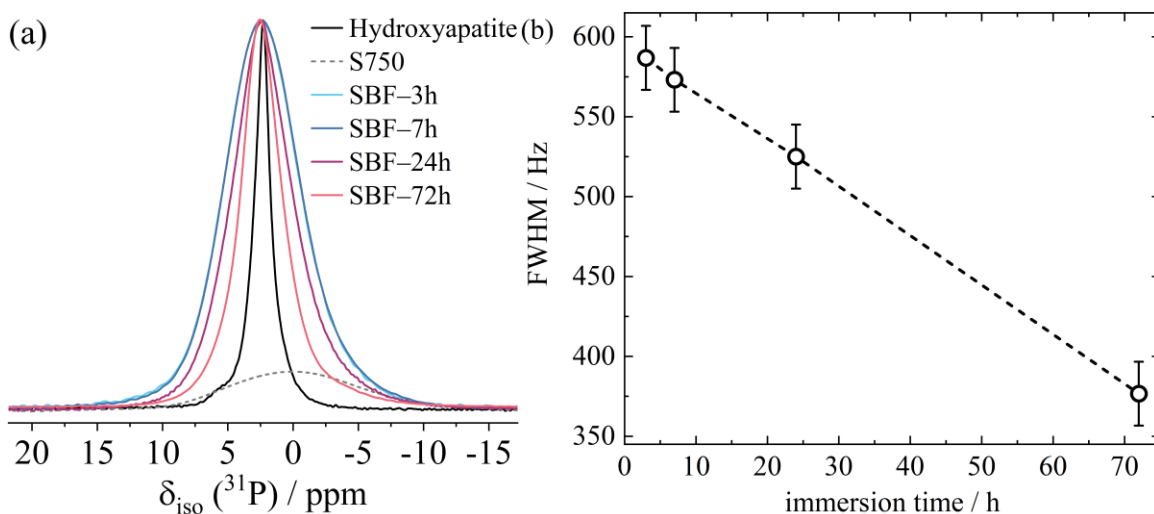
Figure 10: (a) ^{31}P MAS NMR spectra of pristine hydroxyapatite (black) and S750 before (gray dotted line) and after immersion in SBF. (b) Linewidth dependency of the glassy calcium phosphate species P_1^g on the immersion time of the SBF-immersed samples. FWHM values and lineshape deconvolution parameters are listed in Table 4.

The width and shape of the observed signal are due to the formation of amorphous hydrogenated phosphate species with substantially broadened line widths preceding the crystallization of HA [46,48]. As the immersion time is increased, the linewidth decreases since the amorphous phosphate species are converted to nanocrystalline HA.

Hahn-Echo ^{1}H MAS NMR and 2D [31]P(^{1}H) HETCOR MAS NMR spectra of SBF-72h are shown in Figure 11. The ^{1}H echo spectra, shown in Figure 11(a), feature three distinct signals: One broad signal at 4.8 ppm corresponding to water and another shoulder at -0.3 ppm, which is usually assigned to hydroxide ions [45,47,48]. As the HETCOR MAS NMR spectrum in Figure 11(b) confirms, both sites are in proximity to the precipitated orthophosphate, confirming the formation of amorphous HA phases surrounded by surface-bound water.
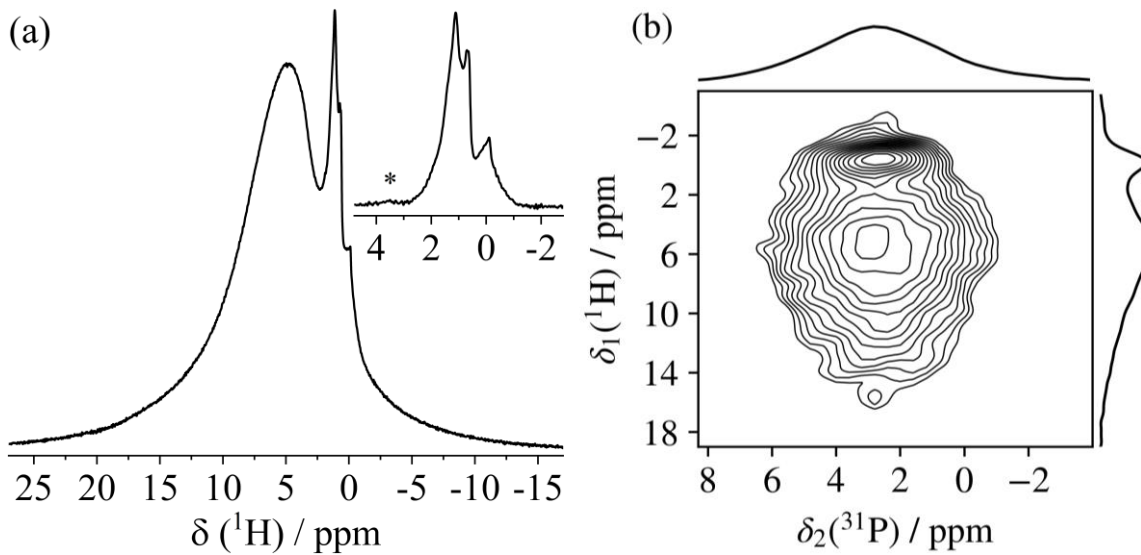
Figure 11: (a) Hahn-echo ^{1}H MAS NMR spectrum of SBF-72h, using an echo delay time of 2 τ_{MAS} (160 us). The inset shows the Hahn-echo ^{1}H MAS NMR spectrum, using an echo length of 20 τ_{MAS} (1600 us). The asterisk indicates an impurity, possibly due to protonated calcium hydroxide surface sites [49] (b) 2D ^{31}P{^{1}H} HETCOR MAS NMR spectrum of SBF-72h, using a contact time of 3.0 ms.

Another group of signals consists of two sharp lines at 1.1 ppm and 0.7 ppm. While similar signals have also been observed in HA particles [45,47,48] and for other SBF-immersed glass formations [37], they do not give rise to correlation signals in the 2D ^{31}P{^{1}H} HETCOR MAS NMR spectrum shown in Figure 11(b). Hence, these signals are assigned to organic residues [47,50].

The obtained quantitative ^{31}P MAS NMR spectra in Figure 10(a) are deconvolved under consideration of at least three different components, which are all assumed to consist solely of orthophosphate (Q^0) units based on their chemical shift and absence of chemical shift anisotropy: (1) "glassy" phosphate owing to disordered, water-containing calcium phosphates, designated as P_1^g, (2) a secondary amorphous hydrogen phosphate species (P_2^g) causing the asymmetric line shape for all SBF-immersed samples and (3) crystalline bulk HA (P_1^{HA}) [45,46]. For immersion times of 24 h and 72 h, the lattermost, crystalline component P_1^{HA} is required to satisfactorily reconstruct the obtained ^{31}P MAS NMR spectra, while for shorter immersion times, two glassy components are already sufficient (see fit parameters below). Lastly, P_2^{HA} is not considered for

lineshape deconvolution of the SBF-immersed S750 signals due to its low intensity relative to P_1^{HA} in the pristine HA sample.

This deconvolution procedure leads to the fit parameters shown in Table 4 (with corresponding lineshape deconvolutions of all samples shown in Figure S7). The fit parameters indicate that the observed shoulder P_2^g only makes up a few percent of the total signal intensity. Furthermore, the crystalline HA component only becomes significant for immersion times of 24 h or higher, reaching ~9% for SBF-72h.

The linewidth of the observed species decreases in a strongly linear fashion, as is shown by the diagram in Figure 10(b) relating the immersion time to the full width at half maximum of the P_1^g species. Over time, the observed phosphate species (including the crystalline HA) underwent decomposition, giving rise to sharp peaks with markedly lower longitudinal relaxation times. An exemplary ^{31}P NMR MAS spectrum after decomposition is shown in Figure S8, indicating non-glassy Q^0 residues at $\delta_{iso} = -0.3$ ppm and $\delta_{iso} = -4.8$ ppm.

Table 4: Isotropic shift δ_{iso}, peak areas f, and mixed Gauss-Lorentz linewidth lb obtained from deconvolution of S750 before and after immersion. All species are assigned to Q^0 (orthophosphate) units. [a] For $f < 1\%$, the respective site is considered not detectable in the respective sample.

	Assignment	δ_{iso} / ppm (± 0.1)	f / % ($\pm 2\%$)	lb / Hz (± 20)
S750	P^g	-0.1	100	2410
Hydroxyapatite	P_1^{HA}	2.3	99	120
	P_2^{HA}	5.5	1	80
SBF-3h	P_1^g	2.5	95	590
	P_2^g	-2.5	5	540
	P_1^{HA}	--	<1 [a]	--
SBF-7h	P_1^g	2.5	92	580
	P_2^g	-2.5	7	620
	P_1^{HA}	2.5	<1 [a]	120
SBF-24h	P_1^g	2.5	90	530
	P_2^g	-2.5	5	520
	P_1^{HA}	2.5	5	130
SBF-72h	P_1^g	2.5	91	380
	P_2^g	--	<1 [a]	--

| | P_1^{HA} | 2.6 | 9 | 160 |

Cell viability tests

The MTT assay results presented in Figure 12(a-c) demonstrate that using urea and sucrose as fuels during the synthesis process did not negatively affect the growth and proliferation of 3T3 cells. This is evident from the consistent cell viability observed across different concentrations (0.5, 1, and 2.5 mg/mL) of the synthesized samples after 1-day post-incubation. However, an increase in the concentration of the glass powders resulted in a decrease in cell proliferation, which could be attributed to the higher concentration of boron ions released in the medium. Overall, these findings together with the rapid formation of HA suggest that the glass powders are favorable for tissue engineering applications.
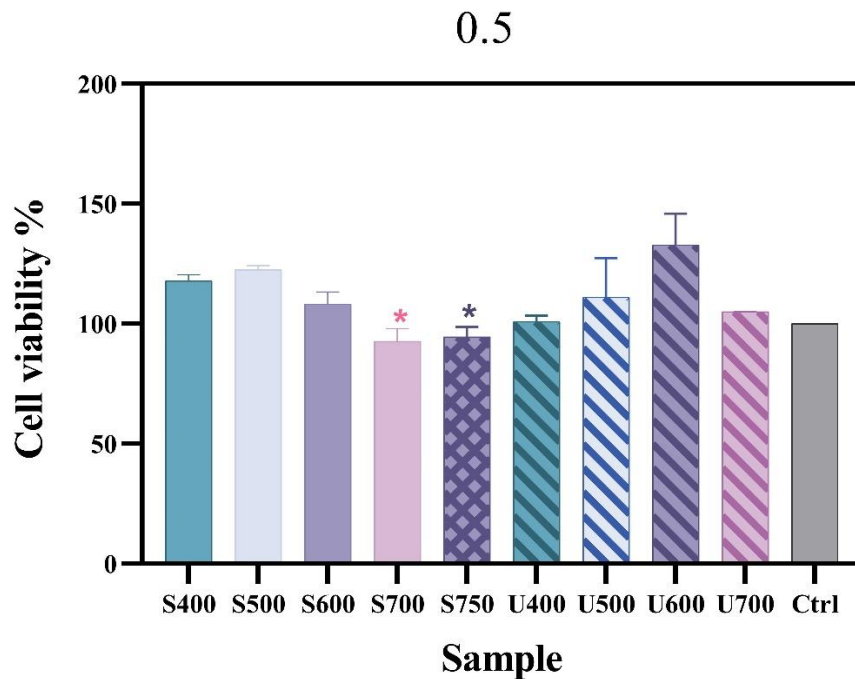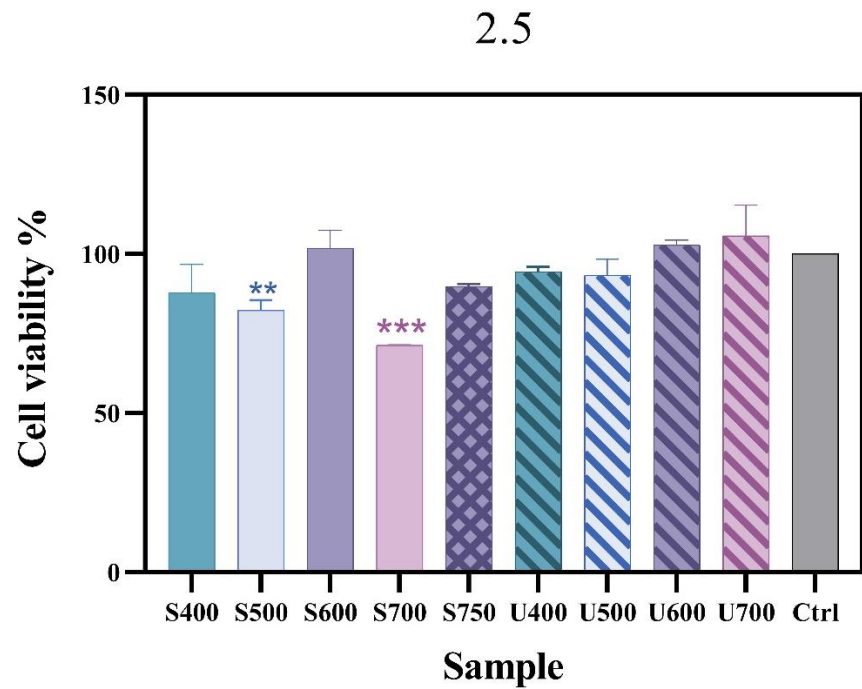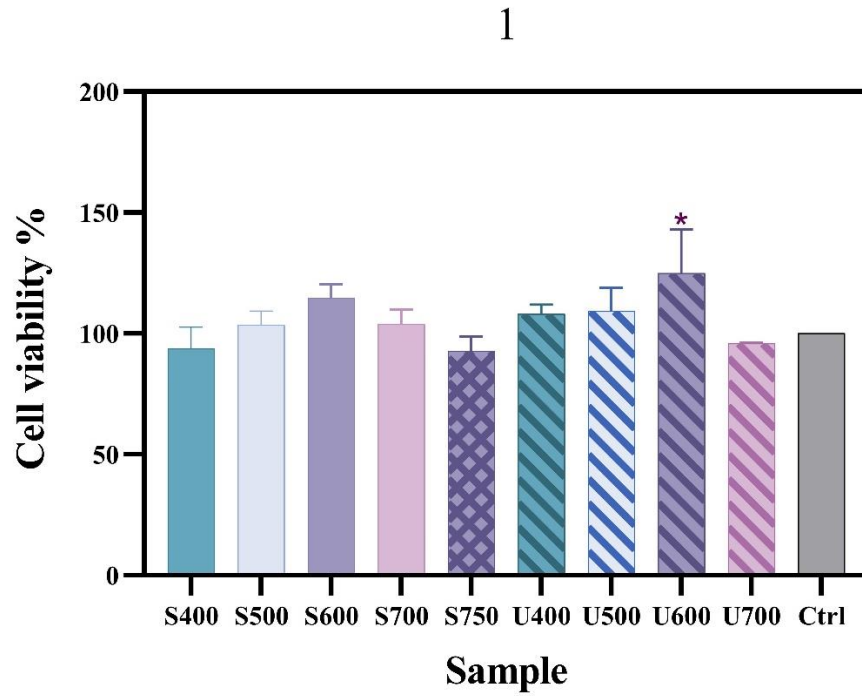
Figure 12. Results of MTT assay for the conditioned medium containing a) 0.5 mg/mL of the glass powders, b) 1 mg/mL of the glass powders, and c) 2.5 mg/mL of the glass powders after 24 hours.

4. Conclusion

The present study investigated the microstructural properties, dissolution behavior, and hydroxyapatite (HA) formation of borate-based bioactive 13-93B3 glasses prepared via the SCS method in the presence of urea and sucrose as fuels at different furnace temperatures (T_0). Adsorption measurements (BET/BJH) demonstrated the mesoporous character of the samples, and DLS showed that a large percentage of the glass particles exhibit a size below 100 nm, depending on the reaction temperature. For threshold temperatures above 700 and 750°C for the urea and sucrose systems, respectively, some sintering occurs, resulting in larger particles generally. ICP-OES measurements further provided evidence that the increased ion release rates can be attributed to the small particle size and high surface areas. After immersion in simulated body fluid (SBF), the formation of an amorphous orthophosphate phase was evidenced by ^{31}P MAS NMR and 2D $^{31}P\{^{1}H\}$HETCOR NMR, which partially crystallizes to HA over the course of three days, as confirmed by XRD. In the present case, samples with larger particle sizes (U/S700) lead to the formation of a moderately higher amount of larger HA crystallites after three days of immersion in SBF compared to those with smaller PSDs (U/S600 and below), which produce nanoscopic HA crystals, clearly evidenced by the width of the XRD bands. Lastly, the high HA formation rate, as well as the results of MTT assays, demonstrated the in vitro biocompatibility of the glass powders. The ability to form a crystalline phase similar to that of natural bone minerals and the biocompatibility of the samples make them an attractive option for biomedical research. However, future work should aim to further understand the relationship between combustion temperature and structure to enable the tailoring of dissolution rates, which is highly desirable for in vivo applications of these glasses.

5. Conflicts of interest

There are no conflicts to declare.

6. Acknowledgments

References

[1]   L.L. Hench, R.J. Splinter, W.C. Allen, T.K. Greenlee, Bonding mechanisms at the interface of ceramic prosthetic materials, J Biomed Mater Res. 5 (1971). https://doi.org/10.1002/jbm.820050611.

[2]   L.L. Hench, Bioceramics: From Concept to Clinic, Journal of the American Ceramic Society. 74 (1991). https://doi.org/10.1111/j.1151-2916.1991.tb07132.x.

[3]   D.S. Brauer, D. Möncke, Chapter 3: Introduction to the Structure of Silicate, Phosphate and Borate Glasses, in: RSC Smart Materials, 2017. https://doi.org/10.1039/9781782622017-00061.

[4]   L.L. Hench, The story of Bioglass®, in: J Mater Sci Mater Med, 2006. https://doi.org/10.1007/s10856-006-0432-z.

[5]   J.R. Jones, D.S. Brauer, L. Hupa, D.C. Greenspan, Bioglass and Bioactive Glasses and Their Impact on Healthcare, Int J Appl Glass Sci. 7 (2016). https://doi.org/10.1111/ijag.12252.

[6]   J.R. Jones, Reprint of: Review of bioactive glass: From Hench to hybrids, Acta Biomater. 23 (2015). https://doi.org/10.1016/j.actbio.2015.07.019.

[7]   A.A. El-Rashidy, J.A. Roether, L. Harhaus, U. Kneser, A.R. Boccaccini, Regenerating bone with bioactive glass scaffolds: A review of in vivo studies in bone defect models, Acta Biomater. 62 (2017). https://doi.org/10.1016/j.actbio.2017.08.030.

[8]   M.C. Crovace, M.T. Souza, C.R. Chinaglia, O. Peitl, E.D. Zanotto, Biosilicate® - A multipurpose, highly bioactive glass-ceramic. in vitro, in vivo and clinical trials, J Non Cryst Solids. 432 (2016). https://doi.org/10.1016/j.jnoncrysol.2015.03.022.

[9]   Q. Fu, E. Saiz, M.N. Rahaman, A.P. Tomsia, Bioactive glass scaffolds for bone tissue engineering: State of the art and future perspectives, Materials Science and Engineering C. 31 (2011). https://doi.org/10.1016/j.msec.2011.04.022.

[10]   V. Miguez-Pacheco, L.L. Hench, A.R. Boccaccini, Bioactive glasses beyond bone and teeth: Emerging applications in contact with soft tissues, Acta Biomater. 13 (2015). https://doi.org/10.1016/j.actbio.2014.11.004.

[11]   F. Baino, G. Novajra, V. Miguez-Pacheco, A.R. Boccaccini, C. Vitale-Brovarone, Bioactive glasses: Special applications outside the skeletal system, J Non Cryst Solids. 432 (2016). https://doi.org/10.1016/j.jnoncrysol.2015.02.015.

[12]   V. Miguez-Pacheco, A.A. Gorustovich, A.R. Boccaccini, J.A. Roether, Chapter 15: Bioactive Glasses for Soft Tissue Engineering Applications, in: RSC Smart Materials, 2017. https://doi.org/10.1039/9781782622017-00336.

[13]   P. Balasubramanian, T. Büttner, V. Miguez Pacheco, A.R. Boccaccini, Boron-containing bioactive glasses in bone and soft tissue engineering, J Eur Ceram Soc. 38 (2018). https://doi.org/10.1016/j.jeurceramsoc.2017.11.001.

[14]   P. Balasubramanian, L. Hupa, B. Jokic, R. Detsch, A. Grünewald, A.R. Boccaccini, Angiogenic potential of boron-containing bioactive glasses: in vitro study, J Mater Sci. 52 (2017). https://doi.org/10.1007/s10853-016-0563-7.

[15]   Q. Yang, S. Chen, H. Shi, H. Xiao, Y. Ma, In vitro study of improved wound-healing effect of bioactive borate-based glass nano-/micro-fibers, Materials Science and Engineering C. 55 (2015). https://doi.org/10.1016/j.msec.2015.05.049.

[16]   S. Naseri, W.C. Lepry, S.N. Nazhat, Bioactive glasses in wound healing: Hope or hype?, J Mater Chem B. 5 (2017). https://doi.org/10.1039/c7tb01221g.

[17]   T. Kokubo, H. Takadama, How useful is SBF in predicting in vivo bone bioactivity?, Biomaterials. 27 (2006). https://doi.org/10.1016/j.biomaterials.2006.01.017.

[18]   P. Sepulveda, J.R. Jones, L.L. Hench, Effect of particle size on bioglass dissolution, Key Eng Mater. 192–195 (2001).

[19]   A. Varma, A.S. Mukasyan, A.S. Rogachev, K. V. Manukyan, Solution Combustion Synthesis of Nanoscale Materials, Chem Rev. 116 (2016). https://doi.org/10.1021/acs.chemrev.6b00279.

[20]   N. Stone-Weiss, H. Bradtmüller, H. Eckert, A. Goel, Composition-Structure-Solubility Relationships in Borosilicate Glasses: Toward a Rational Design of Bioactive Glasses with Controlled Dissolution Behavior, ACS Appl Mater Interfaces. 13 (2021). https://doi.org/10.1021/acsami.1c07519.

[21]   C. Vinod Chandran, P.K. Madhu, N.D. Kurur, T. Bräuniger, Swept-frequency two-pulse phase modulation (SWf-TPPM) sequences with linear sweep profile for heteronuclear decoupling in solid-state NMR, Magnetic Resonance in Chemistry. 46 (2008). https://doi.org/10.1002/mrc.2285.

[22]   G. Kaur, G. Pickrell, N. Sriranganathan, V. Kumar, D. Homa, Review and the state of the art: Sol–gel and melt quenched bioactive glasses for tissue engineering, J Biomed Mater Res B Appl Biomater. 104 (2016). https://doi.org/10.1002/jbm.b.33443.

[23]   G. Kaur, G. Pickrell, G. Kimsawatde, D. Homa, H.A. Allbee, N. Sriranganathan, Synthesis, cytotoxicity, and hydroxyapatite formation in 27-Tris-SBF for sol-gel based CaO-P2O5-SiO2-B2O 3-ZnO bioactive glasses, Sci Rep. 4 (2014). https://doi.org/10.1038/srep04392.

[24]   G. Kaur, O.P. Pandey, K. Singh, D. Homa, B. Scott, G. Pickrell, A review of bioactive glasses: Their structure, properties, fabrication and apatite formation, J Biomed Mater Res A. 102 (2014). https://doi.org/10.1002/jbm.a.34690.

[25]   J. Chevalier, L. Gremillard, Ceramics for medical applications: A picture for the next 20 years, J Eur Ceram Soc. 29 (2009). https://doi.org/10.1016/j.jeurceramsoc.2008.08.025.

[26]   W.C. Lepry, S.N. Nazhat, Highly Bioactive Sol-Gel-Derived Borate Glasses, Chemistry of Materials. 27 (2015). https://doi.org/10.1021/acs.chemmater.5b01697.

[27]   W.C. Lepry, S.N. Nazhat, A Review of Phosphate and Borate Sol–Gel Glasses for Biomedical Applications, Adv Nanobiomed Res. 1 (2021). https://doi.org/10.1002/anbr.202000055.

[28]   M. Ghanad, N. Akrami, P. Keil, H. Bradtmüller, M.R. Hansen, J.V. Khaki, S.M. Beidokhti, Single-step solution combustion synthesis of porous 1393-B3 glass powders and structural characterization via solid-state NMR spectroscopy, Ceram Int. (2023). https://doi.org/https://doi.org/10.1016/j.ceramint.2023.01.061.

[29]   A.V. Saghir, S.M. Beidokhti, J.V. Khaki, A. Salimi, One-step synthesis of single-phase (Co, Mg, Ni, Cu, Zn) O High entropy oxide nanoparticles through SCS procedure: Thermodynamics and experimental evaluation, J Eur Ceram Soc. 41 (2021). https://doi.org/10.1016/j.jeurceramsoc.2020.08.044.

[30]   E. Novitskaya, J.P. Kelly, S. Bhaduri, O.A. Graeve, A review of solution combustion synthesis: an analysis of parameters controlling powder characteristics, International Materials Reviews. 66 (2021). https://doi.org/10.1080/09506608.2020.1765603.

[31]   C. Jaeger, F. Hemmann, EASY: A simple tool for simultaneously removing background, deadtime and acoustic ringing in quantitative NMR spectroscopy. Part II: Improved ringing suppression, application to quadrupolar nuclei, cross polarisation and 2D NMR, Solid State Nucl Magn Reson. 63 (2014). https://doi.org/10.1016/j.ssnmr.2014.08.001.

[32]   C. Jaeger, F. Hemmann, EASY: A simple tool for simultaneously removing background, deadtime and acoustic ringing in quantitative NMR spectroscopy - Part I: Basic principle and applications, Solid State Nucl Magn Reson. 57–58 (2014). https://doi.org/10.1016/j.ssnmr.2013.11.002.

[33]   G. Metz, X. Wu, S.O. Smith, Ramped-Amplitude Cross Polarization in Magic-Angle-Spinning NMR, J Magn Reson A. 110 (1994). https://doi.org/10.1006/jmra.1994.1208.

[34]   D.P. Burum, Cross Polarization in Solids, EMagRes. 2007 (2007). https://doi.org/10.1002/9780470034590.emrstm0103.

[35]   D. Marion, M. Ikura, R. Tschudin, A. Bax, Rapid recording of 2D NMR spectra without phase cycling. Application to the study of hydrogen exchange in proteins, Journal of Magnetic Resonance (1969). 85 (1989). https://doi.org/10.1016/0022-2364(89)90152-2.

[36]   S.G.J. van Meerten, W.M.J. Franssen, A.P.M. Kentgens, ssNake: A cross-platform open-source NMR data processing and fitting application, Journal of Magnetic Resonance. 301 (2019). https://doi.org/10.1016/j.jmr.2019.02.006.

[37]   K. Schuhladen, X. Wang, L. Hupa, A.R. Boccaccini, Dissolution of borate and borosilicate bioactive glasses and the influence of ion (Zn, Cu) doping in different solutions, J Non Cryst Solids. 502 (2018). https://doi.org/10.1016/j.jnoncrysol.2018.08.037.

[38]   F. Kermani, H. Sadidi, A. Ahmadabadi, S.J. Hoseini, S.H. Tavousi, A. Rezapanah, S. Nazarnezhad, S.A. Hosseini, S. Mollazadeh, S. Kargozar, Modified Sol-Gel Synthesis of Mesoporous Borate Bioactive Glasses for Potential Use in Wound Healing, Bioengineering (Basel). 9 (2022). https://doi.org/10.3390/BIOENGINEERING9090442.

[39]   W.C. Lepry, S.N. Nazhat, The anomaly in bioactive sol-gel borate glasses, Mater Adv. 1 (2020). https://doi.org/10.1039/d0ma00360c.

[40] S. Naseri, W.C. Lepry, V.B. Maisuria, N. Tufenkji, S.N. Nazhat, Development and characterization of silver-doped sol-gel-derived borate glasses with anti-bacterial activity, J Non Cryst Solids. 505 (2019). https://doi.org/10.1016/j.jnoncrysol.2018.11.026.

[41] J. Rouquerol, D. Avnir, D.H. Everett, C. Fairbridge, M. Haynes, N. Pernicone, J.D.F. Ramsay, K.S.W. Sing, K.K. Unger, Guidelines for the Characterization of Porous Solids, Stud Surf Sci Catal. 87 (1994). https://doi.org/10.1016/S0167-2991(08)63059-1.

[42] X. Liu, M.N. Rahaman, D.E. Day, Conversion of melt-derived microfibrous borate (13-93B3) and silicate (45S5) bioactive glass in a simulated body fluid, J Mater Sci Mater Med. 24 (2013). https://doi.org/10.1007/s10856-012-4831-z.

[43] F.D. Haghighi, S.M. Beidokhti, Z.T. Najaran, S. Sahebian Saghi, Highly improved biological and mechanical features of bioglass-ceramic/ gelatin composite scaffolds using a novel silica coverage, Ceram Int. 47 (2021). https://doi.org/10.1016/j.ceramint.2021.01.274.

[44] W. Huang, D.E. Day, K. Kittiratanapiboon, M.N. Rahaman, Kinetics and mechanisms of the conversion of silicate (45S5), borate, and borosilicate glasses to hydroxyapatite in dilute phosphate solutions, J Mater Sci Mater Med. 17 (2006). https://doi.org/10.1007/s10856-006-9220-z.

[45] C. Jäger, T. Welzel, W. Meyer-Zaika, M. Epple, A solid-state NMR investigation of the structure of nanocrystalline hydroxyapatite, Magnetic Resonance in Chemistry. 44 (2006). https://doi.org/10.1002/mrc.1774.

[46] D.L. Trandafir, C. Mirestean, R.V.F. Turcu, B. Frentiu, D. Eniu, S. Simon, Structural characterization of nanostructured hydroxyapatite-iron oxide composites, Ceram Int. 40 (2014). https://doi.org/10.1016/j.ceramint.2014.03.124.

[47] T. Isobe, S. Nakamura, R. Nemoto, M. Senna, H. Sfihi, Solid-state double nuclear magnetic resonance study of the local structure of calcium phosphate nanoparticles synthesized by a wet-mechanochemical reaction, Journal of Physical Chemistry B. 106 (2002). https://doi.org/10.1021/jp0138936.

[48] E.E. Wilson, A. Awonusi, M.D. Morris, D.H. Kohn, M.M.J. Tecklenburg, L.W. Beck, Three structural roles for water in bone observed by solid-state NMR, Biophys J. 90 (2006). https://doi.org/10.1529/biophysj.105.070243.

[49] D.E. Sandström, M. Jarlbring, O.N. Antzutkin, W. Forsling, A spectroscopic study of calcium surface sites and adsorbed iron species at aqueous fluorapatite by means of ^1H and ^{31}P MAS NMR, Langmuir. 22 (2006). https://doi.org/10.1021/la0602158.

[50] P.N. Gunawidjaja, A.Y.H. Lo, I. Izquierdo-Barba, A. García, D. Arcos, B. Stevensson, J. Grins, M. Vallet-Regí, M. Edén, Biomimetic apatite mineralization mechanisms of mesoporous bioactive glasses as probed by multinuclear ^{31}P,^{29}Si,^{23}Na and ^{13}C solid-state NMR, Journal of Physical Chemistry C. 114 (2010). https://doi.org/10.1021/jp105408c.
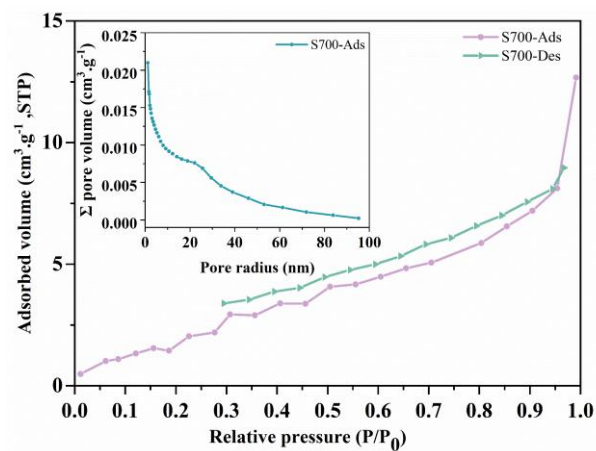
Supporting information
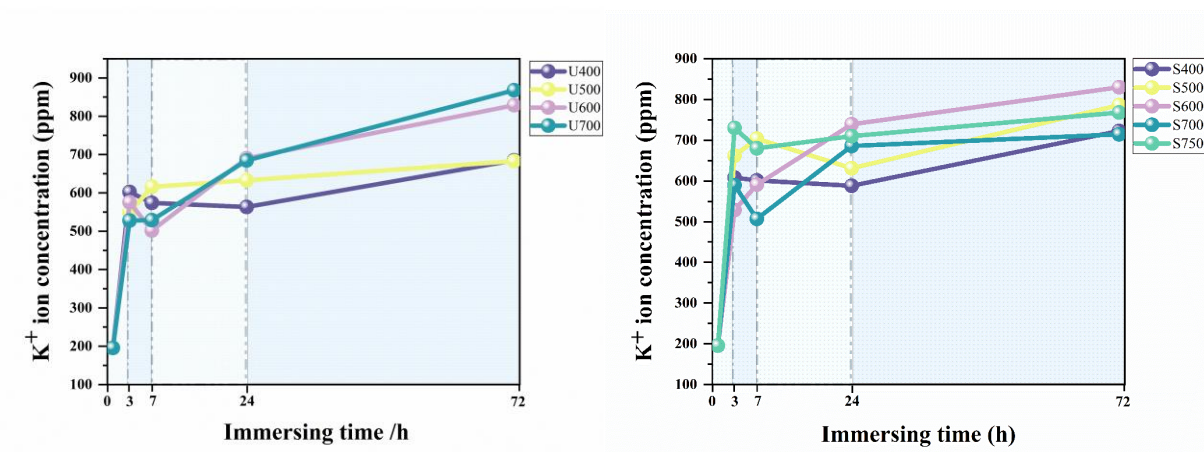

Figure S1. BET results of S700 sample.

Figure S2. K^+ ion concentration of synthesized glass powders in the presence of urea (left) and sucrose (right). (purple=X400, yellow=X500, pink=X600, blue=X700, green=X750, with X = U, S)
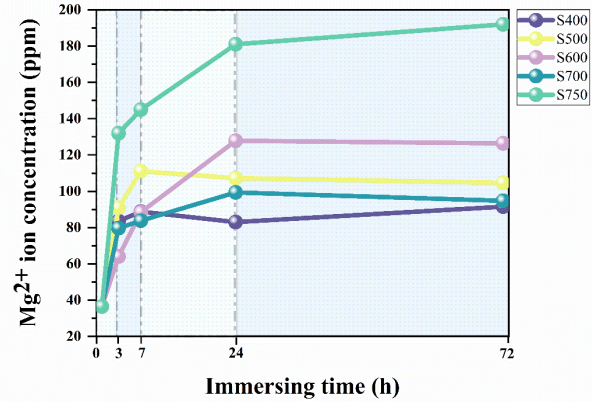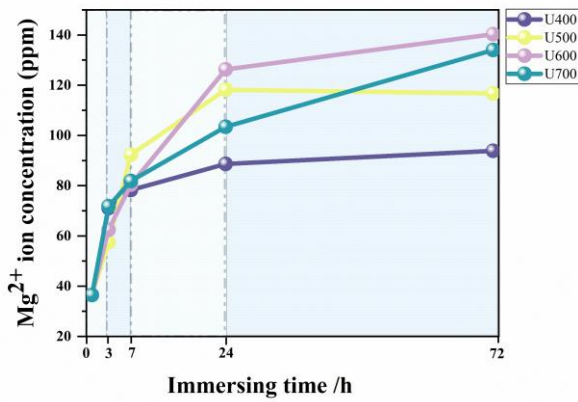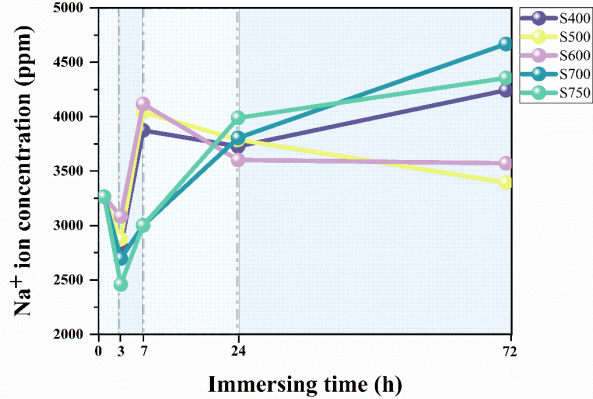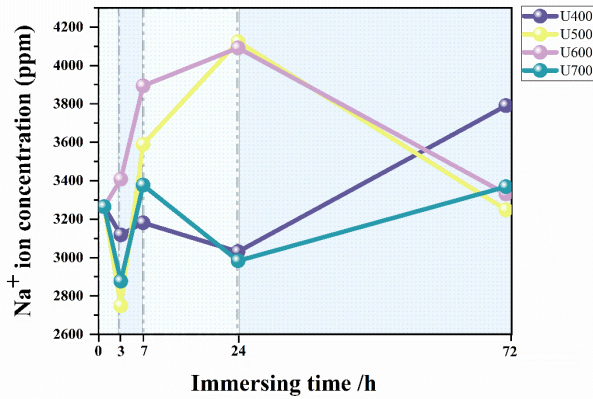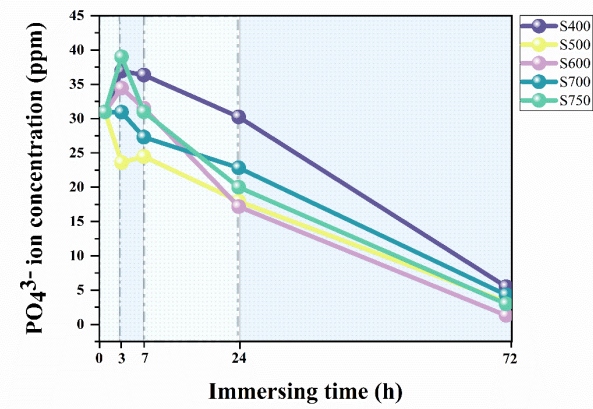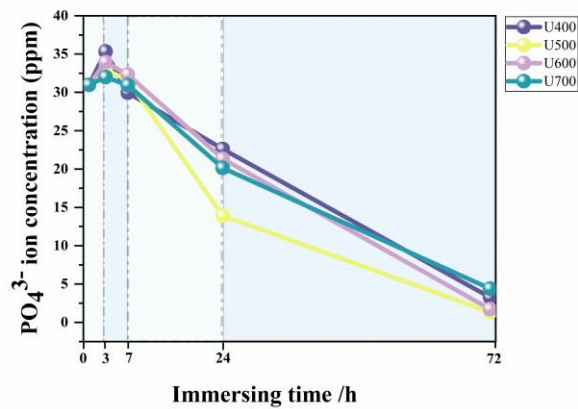
Figure S3. Mg^{2+} ion concentration of synthesized glass powders in the presence of urea (left) and sucrose (right). (purple=X400, yellow=X500, pink=X600, blue=X700, green=X750, with X = U, S)
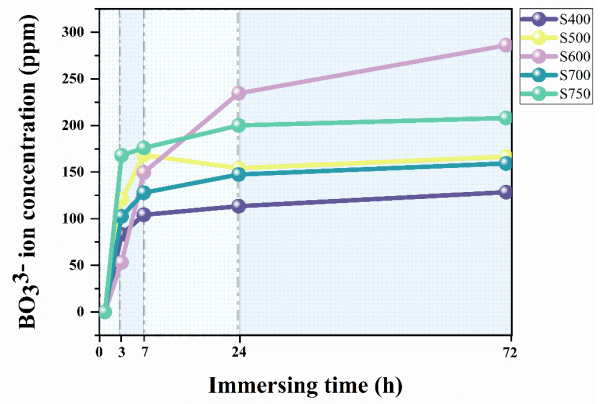

Figure S4. Na$^+$ ion concentration of synthesized glass powders in the presence of urea (left) and sucrose (right). (purple=X400, yellow=X500, pink=X600, blue=X700, green=X750, with X = U, S)
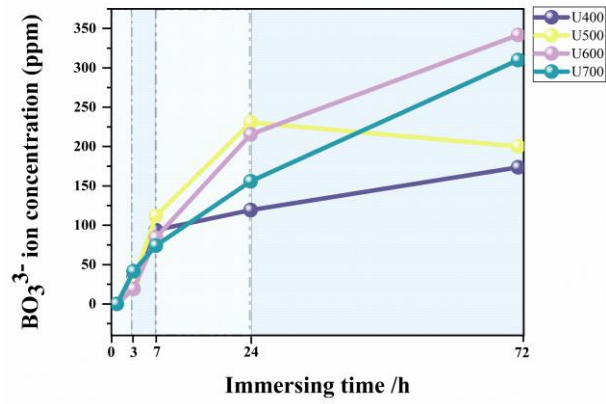

Figure S5. PO$_4^{3-}$ ion concentration of synthesized glass powders in the presence of urea (left) and sucrose (right). (purple=X400, yellow=X500, pink=X600, blue=X700, green=X750, with X = U, S)

Figure S6. BO_3^{3-} ion concentration of synthesized glass powders in the presence of urea (left) and sucrose (right). (purple=X400, yellow=X500, pink=X600, blue=X700, green=X750, with X = U, S)

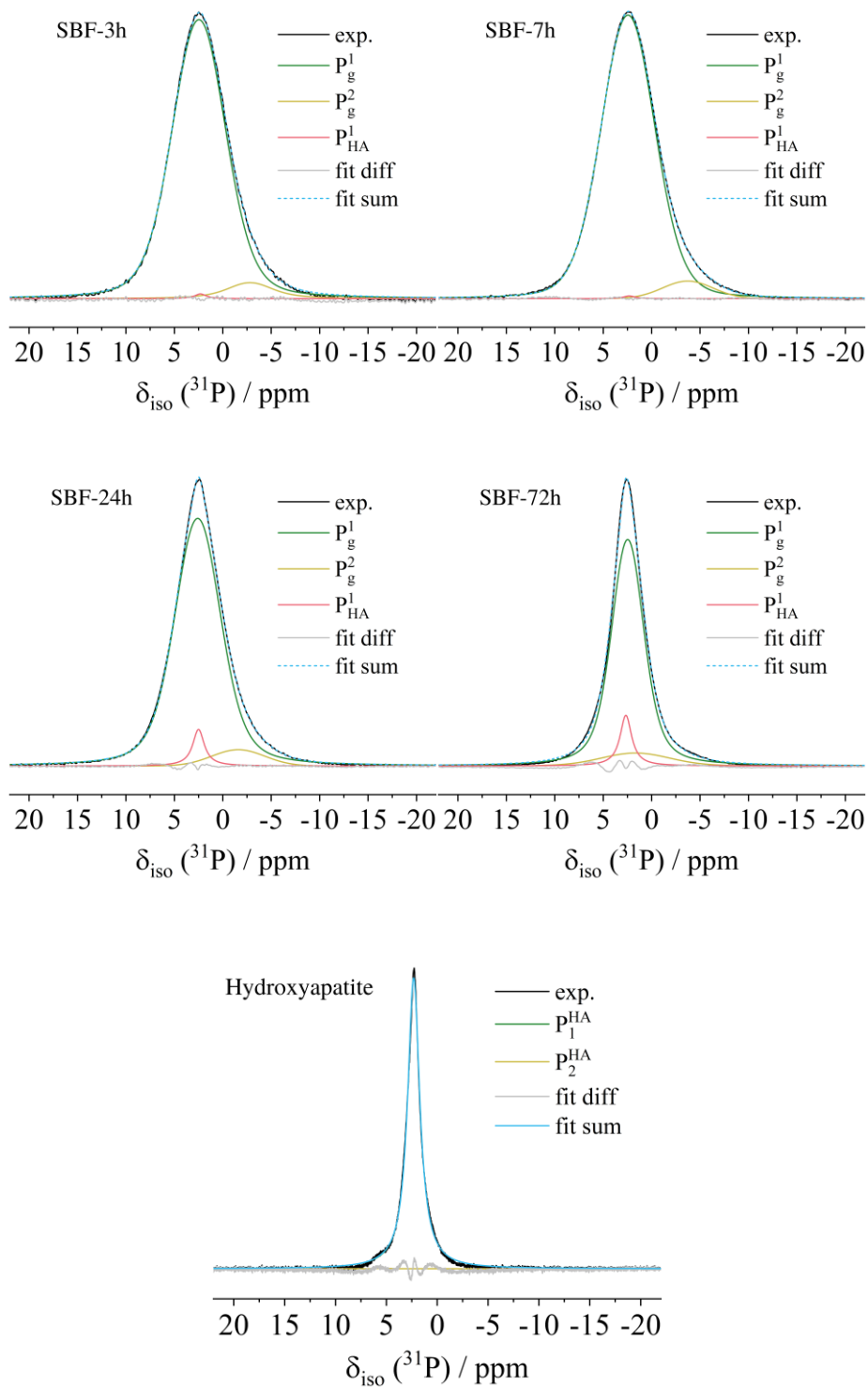## S2 Deconvolutions of ^{31}P MAS NMR spectra obtained for SBF-immersed S750

Figure S7: Deconvolutions of the ^{31}P MAS NMR spectra of pristine Hydroxyapatite and S750 after SBF immersion. The deconvolution parameters are given in Table 3.

S2 ³¹P MAS NMR spectra after HA decomposition at atmospheric conditions

S2 ^{31}P MAS NMR spectra after HA decomposition at atmospheric conditions
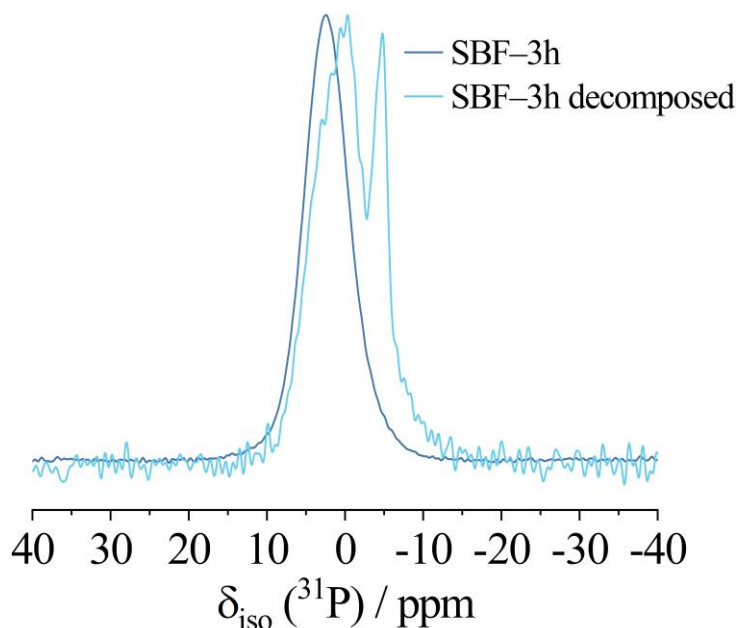

Figure S8: Comparison of ^{31}P MAS NMR spectra before (dark blue) and after HA (light blue) decomposition at atmospheric conditions. For the signal after decomposition, 256 scans were recorded using a recycle delay of 2 s. The peaks were normalised to maximum intensity.

S3 ^{11}B MAS EASY spectra of SBF-3h and SBF-72h

The ^{11}B spectra of SBF-3h and SBF-72h are shown in Figure S9. As already indicated by the ICP results in Figure S6, significant leaching of the borate network takes place during dissolution. For SBF-3h, the signal of the trigonal B3 species is strongly decayed and disappeared completely for SBF-72h.
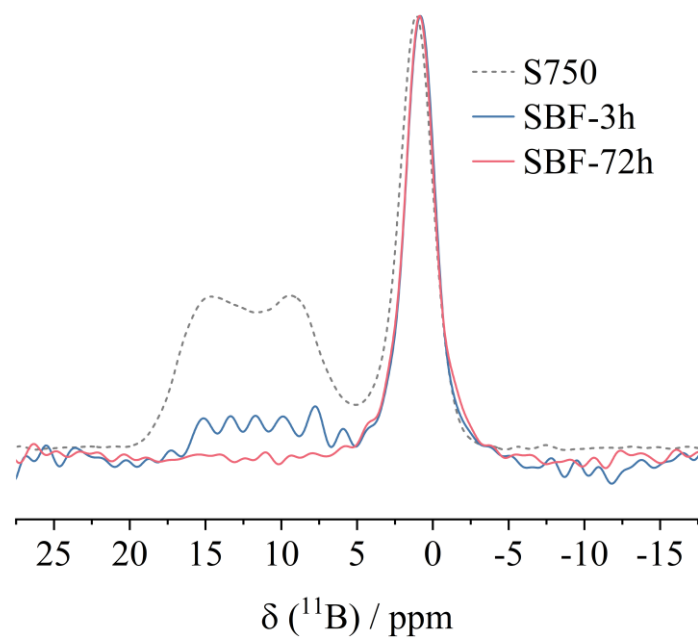
Figure S9: ^{11}B EASY MAS NMR spectra of untreated S750 (grey, dotted line) and after 3h (blue) and 72h (red) of immersion in SBF. The peaks were normalised to the intensity of the B^4 signal.